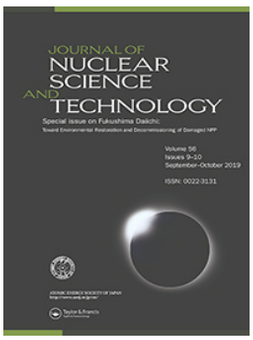

Journal of Nuclear Science and Technology

ISSN: 0022-3131 (Print) 1881-1248 (Online) Journal homepage: https://www.tandfonline.com/loi/tnst20

Reactive spark plasma sintering of Cs-exchanged chabazite: characterisation and durability assessment for Fukushima Daiichi NPP clean-up

Liam. C. Harnett, Laura. J. Gardner, Shi-Kuan Sun, Colleen Mann & Neil. C. Hyatt

To cite this article: Liam. C. Harnett, Laura. J. Gardner, Shi-Kuan Sun, Colleen Mann & Neil. C. Hyatt (2019) Reactive spark plasma sintering of Cs-exchanged chabazite: characterisation and durability assessment for Fukushima Daiichi NPP clean-up, Journal of Nuclear Science and Technology, 56:9-10, 891-901, DOI: 10.1080/00223131.2019.1602484

To link to this article: https://doi.org/10.1080/00223131.2019.1602484

Published online: 14 Apr 2019.

JOURNAL OF NUCLEAR SCIENCE AND TECHNOLOGY
2019, VOL. 56, NOS. 9–10, 891–901
https://doi.org/10.1080/00223131.2019.1602484

ARTICLE

Reactive spark plasma sintering of Cs-exchanged chabazite: characterisation and durability assessment for Fukushima Daiichi NPP clean-up

Liam. C. Harnett, Laura. J. Gardner, Shi-Kuan Sun, Colleen Mann and Neil. C. Hyatt

Immobilisation Science Laboratory, Department of Materials Science and Engineering, University of Sheffield, Sheffield, UK

ABSTRACT

Ion-specific media (ISM) have played an integral role in the clean-up and remediation efforts at the Fukushima Dai-ichi disaster site, through the processing of contaminated wastewaters. The use of these materials generates a secondary nuclear waste stream, presenting its own series of engineering problems arising from stringent handling and long-term storage requirements. A reactive spark plasma sintering (SPS) method was investigated for conditioning of the spent cesium exchanged zeolite, chabazite. A natural form of the zeolite was used as an analogue to the engineered ISM used at the Fukushima NPP site. Simulant wasteforms were sintered using different temperature and pressure parameters followed by analysis of phase assemblage, density, and durability (using the product consistency test (PCT)). The results indicated that zeolite structure had collapsed completely, with the exchanged cesium partitioned primarily into a durable feldspar to assure stability of the sintered material for passively safe storage or geological disposal.

ARTICLE HISTORY
Received 21 November 2018
Accepted 23 March 2019

KEYWORDS
Chabazite; zeolite; cesium; reactive spark plasma sintering; Fukushima Daiichi NPP; ion exchange; radioactive waste management

1. Introduction

The March 2011 earthquake and tsunami led to a series of serious coolant loss incidents at the Fukushima Daiichi nuclear power plant (NPP) [1]. Three reactor units experienced partial core meltdowns, but reactor water levels were eventually stabilised by the pumping of sea water and fresh water, achieving cold shutdown conditions. Cesium-137 is a high yield fission product ($t_{½}$ = 31.17 yr) and, consequently, it is present at high concentrations in the NPP wastewater. Due to the radiotoxicity of Cs-137 and other radionuclides present in these effluents, treatment is necessary before the used cooling water can be reused or released.

One method of effluent treatment is the use of ion exchange materials, such as zeolites. These microporous aluminosilicates are available commercially as mineral or synthetic materials, finding common usage in ion exchange as adsorbents. The individually unique structures of these media result in both high selectivity and specificity for ion exchange. To facilitate Cs removal from the contaminated coolant water, one of the main effluent treatment facilities installed on the Fukushima Daiichi NPP site is the KURION ion exchange plant, using engineered Na-chabazite as an exchange medium [2]. The high porosity of this material, based on a ~3.8 Å diameter "8-ring" framework structure, provides a large surface area for exchange with high selectivity for Cs [3,4]. As of October 2018, this facility has treated a cumulative Cs-contaminated water volume of 391,870 m^3, producing 771 large exchange columns of spent material [5]. Conditioning of the large volumes of spent zeolite waste is one of the more demanding unsolved engineering issues as part of the clean-up effort, with strict acceptance criteria and constraints [6] that must be followed: limited space at potential disposal sites necessitates a high reduction in volume of wasteforms, minimal leaching, and corrosion of containment and long-term chemical stability. Vitrification using borosilicate glasses has been considered but volatilisation of cesium at high processing temperatures (up to 1300°C) poses a potential challenge [7]. Encapsulation of ion exchange materials using standard cementitious compositions has been studied [8–10,11], though systems such as ordinary Portland cement (OPC) may necessitate particle size reduction of zeolites, and degradation of the ion exchange framework, as a result of the internal pH, releases the incorporated radiocesium.. Cement encapsulation is also expected to result in arelative volume increase for the final wasteform.

Spark plasma sintering (SPS) is a relatively novel sintering technique that operates on the principle of a Joule heating effect via a very high applied current coupled with uniaxial pressure, which facilitates mass-transport and grain growth. Rapid heating rates and the application of pressure allow near-theoretical densities to be achieved in the final pellet product using relatively low temperatures [12], with the potential for high wasteform volume reduction. This work demonstrates the viability of spark plasma sintering as a method for the thermal

CONTACT Neil. C. Hyatt n.c.hyatt@sheffield.ac.uk Immobilisation Science Laboratory, Department of Materials Science and Engineering, University of Sheffield, Sheffield, UK

treatment of spent chabazite ion exchange materials and evaluates the wasteform chemical durability using the ASTM Product Consistency Test (PCT-B).

2. Experimental methods

2.1 Material synthesis

The chabazite used in this study was a natural source, supplied from Verdi S.p.A as "Zeover." The reported manufacturer data were as follows: the particle size range of 0.1–0.7 mm, a cation exchange capacity (CEC) of 2.2 ± 0.2 meq/g, and a reported composition of $(Na_{0.14}K_{1.03}Ca_{1.00}Mg_{0.17})[Al_{3.46}Si_{8.53}O_{24}]{\cdot}9.7H_2O$ [13]. This constituted a mineral composition of 70 ± 2 wt.% chabazite with minor constituents at: 18 ± 5 wt.% obsidian glass, 5 ± 2 wt.% potassium feldspars, 3 ± 1 wt.% pyroxenes, 2 ± 1 wt.% biotite, and 2 ± 1 wt.% phillipsite [10]. Chabazite was exchanged in a 0.1 M $CsNO_3$ (Arcos Organics, 99% purity) solution using UHQ water (18.2 MΩ). The chabazite was agitated on a roller mill for 24 h at room temperature. The exchanged material was rinsed twice with 1 L of distilled H_2O, filtered, and dried at 95°C for 24 h.

The Cs-chabazite was calcined in air at 300°C for 12 h to remove remnant water. 3 g of the dried Cs-chabazite was pressed into a 20 mm graphite die and consolidated using a HP-D 25 SPS system (FCT Systeme GmBH). The average measured apparent density of green-body pressed pellets was 1.556 ± 0.041 g/cm^3. Samples were consolidated according to the method used by Sun *et al.* [14], at 1000°C or 1100°C at 50°C/min under an argon atmosphere with a dwell time of 10 min, under a uniaxial pressure of 15 MPa or 50 MPa. Sintered samples were allowed to cool naturally to ambient temperature. Residual graphite foil was removed by manual grinding using SiC paper. The total processing time per sample, including die loading, was 60 min.

2.2 Characterisation

The phase assemblage of the as-received, exchanged, and SPS samples was determined by powder X-ray diffraction (XRD) on a Bruker D2 PHASER diffractometer with a LynxEye detector utilising Cu Kα (λ = 1.5418 Å) radiation, a Ni foil was used to filter the Kβ radiation. Diffraction patterns were collected between 5° < 2θ < 50° with a step size of 0.02° 2θ and dwell time of 1 s per step. X-ray fluorescence (XRF) analysis was used to quantify the bulk oxide constituents of the as-received, Cs-exchanged, and SPS samples. XRF beads were prepared using a lithium tetraborate flux (Sigma Aldrich, 99.995% purity) at a 1:10 sample-to-flux ratio and analysed using a PANalytical Zetium spectrometer under vacuum with a Rh tube operating at 50 kV and 30 mA (Table 1). Microstructures were observed using a Hitachi TM3030 scanning electron microscope (SEM) coupled with a Bruker Quantax 70 energy dispersive X-ray spectroscopy system (EDX) at a working distance of 7.4 ± 0.1 mm using a silicon drift detector. Samples were resin mounted, polished to a 1 µm finish, and carbon coated. The approximate stoichiometry was determined on the average composition of 10 EDX data points per microstructural feature. Semi-quantitative phase analysis assumed oxygen stoichiometry required for charge neutrality. Density measurements were conducted using a Micrometrics AccuPyc II 1340 gas pycnometer with a 1 cm^3 sample cell (chabazite samples) and a 0.1 cm^3 cell for the SPS powder for proof of concept studies. The density of the SPS fragments was determined using a Mettler Toledo Archimedes balance (Table 2).

Table 1. Results for compositional analysis by X-ray fluorescence, including calculated values for approximate water loss on ignition and standard deviations for all averaged data.

Compound	As-Received Average (wt.%)	Cs-Exchanged Average (wt.%)	SPS-2 Average (wt.%)
SiO_2	52.10 ± 0.23	50.82 ± 0.02	55.55 ± 0.21
Al_2O_3	18.90 ± 0.03	18.40 ± 0.08	20.45 ± 0.07
K_2O	6.87 ± 0.05	6.60 ± 0.05	7.44 ± 0.03
CaO	6.13 ± 0.01	5.30 ± 0.09	5.46 ± 0.02
Fe_2O_3	5.48 ± 0.02	4.73 ± 0.02	4.28 ± 0.04
MgO	1.98 ± 0.01	1.86 ± 0.02	1.77 ± 0.03
Cs_2O	*	1.96 ± 0.02	2.09 ± 0.20
Na_2O	1.14 ± 0.02	0.73 ± 0.02	0.85 ± 0.03
TiO_2	0.69 ± 0.01	0.62 ± 0.01	0.60 ± 0.01
I	0.44 ± 0.01	0.45 ± 0.01	0.33 ± 0.10
SrO	0.23 ± 0.01	0.20 ± 0.01	0.25 ± 0.05
H_2O **	5.30 ± 0.22	7.76 ± 0.24	*
Total	99.25††	99.45††	99.07††

Below the detection limit

** *Determined by mass loss of structural water upon ignition*

†† *Less than 100% of the composition is reported as the trace components were discounted.*

The chemical durability assessment (sample SPS-2 only) was performed in duplicate using the Product Consistency Test (PCT-B, ASTM methodology C1285-14 [15]). Powdered samples (75–150 µm) were prepared and washed using IPA. Tests were carried out at 90°C in a 15 mL PTFE vessel with 9 mL of leachate (UHQ water, 18.2 MΩ) to give a surface area-to-volume ratio of 1200 m^{-1}, based on geometrical assumptions. Sacrificial samples were taken at time points: 1, 3, 7, 14, 21, and 28 days, aliquots were passed through a 0.2 µm filter, pH measured using a Mettler Toledo pH meter, and acidified with nitric acid (Ultrapure NORMATOM 67–69%, VWR). The leachates were analysed using inductively coupled plasma-optical emission spectroscopy (ICP-OES) (Thermo Fisher iCAPDuo 6300) and ion chromatography (IC) (Thermo Scientific ICS-1100) using the cation column for cesium analysis.

3. Results and discussion

3.1 Exchanged material characterisation

The phase assemblages of the as-received and Cs-exchanged materials were determined by powder XRD (Figure 1). The observed major phases present were

Table 2. The density and phase assemblage reference matrix for all samples in this study.

Sample	Processing Conditions	XRD Phases* Major	XRD Phases* Minor	Main Cs bearing Phase (EDX Formula)	Main Phase Cs (wt.%)	Average Density Archimedes (g/cm^3)	Average Density Gas Pycnometry (g/cm^3)
As-received	–	C	B, K N, P, Q, X	$Ca_{1.5}K_{1.0}$ [$Al_3Si_8O_{24}$]·12H_2O**	-	††	2.4411 ± 0.0015
Cs-exchanged	Cs-exchange	C	B, K, N, P, Q, X	$Cs_{0.5}Ca_{0.9}K_{1.2}$[$Al_4Si_8O_{24}$]·12H_2O**	7.2 ± 3.1	††	2.4679 ± 0.0017
SPS-1	SPS, 1000°C, 10 min, 15MPa	K	B, L, N, Q, X	$Cs_{0.7}Ca_{0.5}K_{1.1}[Al_3Si_8O_{22}]$	11.0 ± 2.8	2.658 ± 0.004	2.6657 ± 0.0038
SPS-2	SPS, 1000°C, 10 min, 50MPa	K	B, L, N, Q, X	$Cs_{0.9}Ca_{0.5}K_{1.1}[Al_3Si_8O_{22}]$	13.7 ± 4.2	2.658 ± 0.003	2.7314 ± 0.0017
SPS-3	SPS, 1100°C, 10 min, 15MPa	K	L, Q, X	$Cs_{0.5}Ca_{0.3}K_{1.6}[Al_3Si_8O_{24}]$	8.4 ± 3.3	2.588 ± 0.003	2.6050 ± 0.0059

* Where: **B** = biotite $KMg_3[AlSi_3O_{10}]$, **C** = chabazite $Ca_2[Al_4Si_8O_{24}]\cdot12H_2O$, **K** = K-feldspars $K[AlSi_3O_8]$, **L** = leucite $K[FeSi_2O_6]$, **N** = anorthite $Ca[Al_2Si_2O_8]$, **P** = phillipsite $Na_2[Al_2SiO_6]\cdot H_2O$, **Q** = quartz [$SiO_2$], and **X** = pyroxene $Fe_{0.07}Na_{0.16}Ca_{0.84}Mg_{0.94}[Si_2O_6]$

** Assuming complete hydration to 12H_2O

†† Not measured as there was only granular sample

chabazite, $Ca_2[Al_4Si_8O_{24}]\cdot12H_2O$ (JCPDS-ICDD, Powder Diffraction File, PDF #34–0137), the K-feldspars $K[AlSi_3O_8]$: sanidine (PDF #71–0992) with microcline (PDF #83–1604), and pyroxene, $Fe_{0.07}Na_{0.16}Ca_{0.84}Mg_{0.94}[Si_2O_6]$ (PDF #86–0005). Several less intense reflections were found to correspond to biotite, $KMg_3[AlSi_3O_{10}]$ (PDF #73–1661), phillipsite, $Na_2[Al_2SiO_6]\cdot12H_2O$ (PDF #12–0195), quartz, [SiO_2] (PDF #81–1665), and anorthite, $Ca[Al_2Si_2O_8]$ (PDF #89–1461). There were only very slight differences between the two diffraction patterns, post Cs-exchange, such as the relative intensities of the low angle reflections for phillipsite, biotite, and chabazite ($2\theta < 20°$), due to Cs ion exchange and preferred orientation effects associated with the biotite mica (where preferred orientation refers to the crystallographic phenomenon of some crystallites having a tendency to pack in favour of a particular direction, influencing the diffraction pattern).

Elemental compositions of the as-received and Cs-exchanged materials were determined using XRF spectroscopy. Table 1 shows the compositions of the pre- and post-exchange samples, by relative average weight percent of oxide components. The water losses, as calculated by the sample mass lost on ignition, had the largest degree of variability, likely resulting from residual water from the exchange process. The large size of the Cs^+ cation means that there is a preferential exchange to the sites of wide ~7Å aperture "8-ring" structure within the chabazite framework [3,4]. XRD and XRF analysis confirm that the bulk mineral and chemical composition is consistent with reference to the manufacturer data sheet.

A BSE micrograph and EDX maps of the Cs-exchanged sample provided a survey of individual particle morphologies and compositions. In Figure 2, a particle with high porosity and grain sizes ranging between 200 and 300 μm was characteristic of a chabazite, and semi-quantitative analysis of a region yielded a composition of $Cs_{0.5}Ca_{0.9}K_{1.2}[Al_4Si_8O_{24}]\cdot12H_2O$, demonstrating the exchange and cation variation on the primary Ca-chabazite (**C**) phase detected by XRD. This corresponds to a Cs loading of 7.2 ± 3.1 wt.% for individual chabazite particles, this is comparable to the Cs-exchange achieved by Du *et al.* for pure chabazite – 6.4 wt.% [16]. A series of angular, low porosity particles were also found, corresponding to K-feldspar (**K**) $K_{0.8}[AlSi_3O_8]$, pyroxene (**X**) $Fe_{0.2}Al_{0.2}Mg_{0.8}Ca_{1.1}[Si_2O_6]$, and a silica/quartz (**Q**) SiO_2. In addition, spherical particles associated with the 18 wt. % ± 5% obsidian glass present within the chabazite source material [13] were observed in the analysis of microstructure, although not apparent in Figure 2 (see Supporting Info 3).

The density of the as-received chabazite (2.4411 ± 0.0015 g/cm^3) was observed to increase after Cs-exchange to 2.4679 ± 0.0017 g/cm^3 (Table 2). This increase is associated with the incorporation of Cs within the chabazite structure, displacing the cation occupancy at the sodium or potassium sites, and increasing the cation atomic mass by ~3–5 fold.

3.2 Characterisation of reactive spark plasma sintered material

Phase assemblages for each of the SPS pellets (SPS-1–3) were determined by powder XRD. The reflections associated with chabazite were entirely absent from the diffraction patterns (Figure 3). This demonstrated that a complete collapse of the zeolite structure was achieved using SPS as a thermal treatment method for ion exchange materials, forming known mineral crystalline phases. The major phases present in all SPS samples were K-feldspars, $K[AlSi_3O_8]$ in the form of sanidine (PDF #83–1657), orthoclase (PDF #83–1253), and microcline (PDF #83–1604), with minor reflections corresponding to anorthite, $Ca[Al_2Si_2O_8]$ (PDF #12–0301) and pyroxene, $Fe_{0.07}Na_{0.16}Ca_{0.84}Mg_{0.94}[Si_2O_6]$ (PDF #86–0005).

Although the SPS-1 (1000°C, 10 min, 15 MPa) and SPS-2 (1000°C, 10 min, 50 MPa) samples had consistent phase assemblages based on the minerals

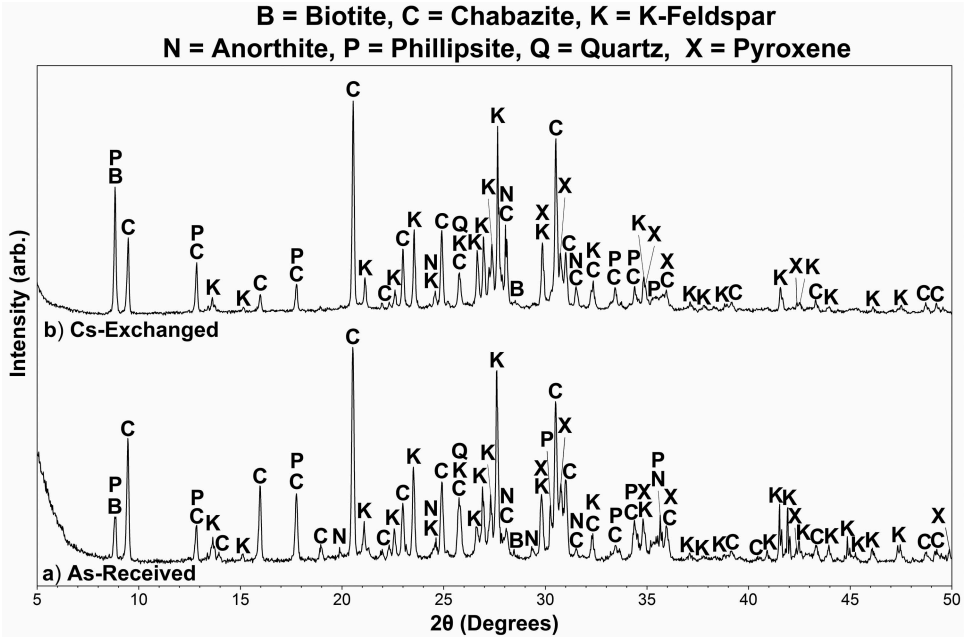

Figure 1. XRD patterns for the (a) as-received and (b) Cs-exchanged samples.

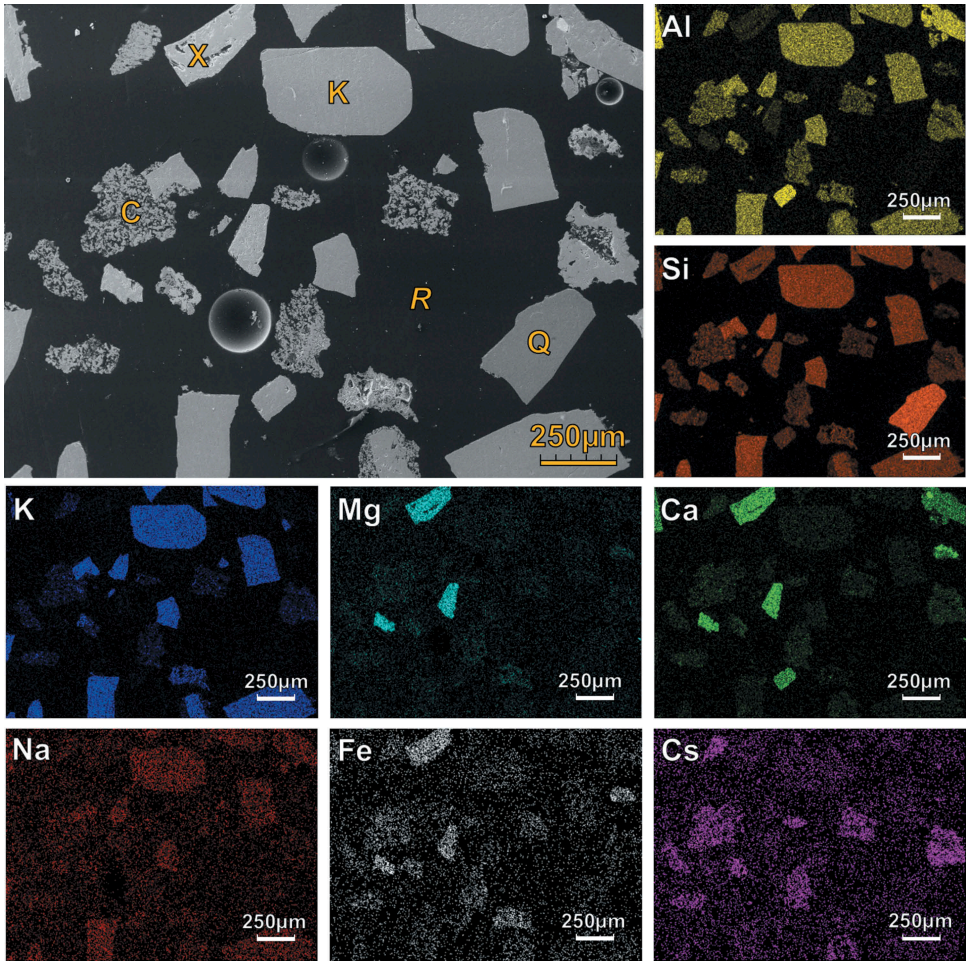

Figure 2. SEM/EDX micrographs of the Cs-exchanged chabazite, where labelled phases correspond to (C) chabazite, (K) potassium feldspar, (Q) quartz, (R) resin, and (X) pyroxene.

present, there were, however, subtle differences in the relative intensities observed. For example, the reflection at 2θ ≈ 27.7°, corresponding to sanidine feldspar (**K**), was observed with a significantly higher relative intensity in the SPS-1 sample, compared to that of the SPS-2. Conversely, the peak at 2θ ≈ 29.3° assigned to anorthite and pyroxene phases (**N**/**X**) had a significantly lower relative intensity in SPS-1.

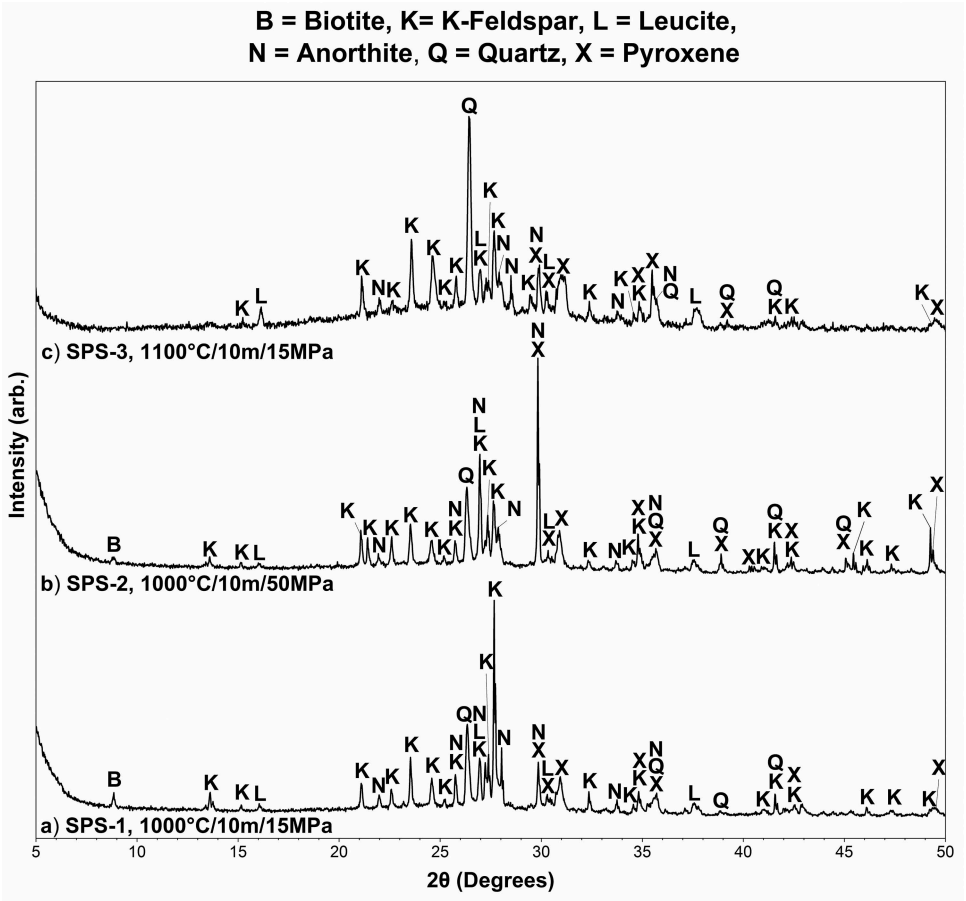

Figure 3. XRD patterns for powdered SPS samples: (a) 1000°C, 10 min, 15 MPa, (b) 1000°C, 10 min, 50 MPa, and (c) 1100°C, 10 min, 15 MPa.

Compared to SPS-1, the effect of an increased processing temperature (SPS-3, 1100°C, 10 min, 15 MPa) resulted in quartz (**Q**) having the highest relative intensity rather than the K-feldspar. Also observed was the emergence of diffuse scattering between $17.5° < 2\theta < 37.5°$. These features are consistent with vitrification mechanisms and amorphous glass phases formed after the complete breakdown of aluminosilicate frameworks [17,18]. Therefore, it is possible to state that for the SPS-processing conditions investigated, the effect of pressure had little impact on the phase assemblage (only the proportion), which was juxtaposed to the effect of temperature. The absence of pollucite ($CsAlSi_2O_6$) was due to the molar ratio of alkali:aluminium:silicon in the SPS composite (approximately 1:2:4.7 – as derived from Table 1), which is closer to the ideal ratio of the feldspar observed in the microstructure (1:1:3) than to that of pollucite (or leucite, the K-counterpart (1: 1: 2)) [19]. The Cs was resultantly taken into the feldspar solid solution during melt crystallisation. The normalised Cs_2O content of the ion exchanged material immediately before and after SPS treatment (i.e. accounting for the loss of water in the calcination pre-treatment step) was determined by XRF analysis to be 2.14 ± 0.02 and 2.11 ± 0.18 wt.%, respectively. No measurable change in the Cs_2O content was determined, within the precision of the analysis, and thus the full inventory of Cs_2O was retained. This is likely due to the very short processing time combined with uniaxial pressure. Further work is required to demonstrate which SPS-processing temperature for waste management of Cs-ion exchange materials is optimal, based on microstructure, chemical stability, and radiation tolerance.

Microstructure and semi-quantitative analysis was undertaken for the SPS pellets, shown in Figures 4–5. The SPS-1 microstructure was observed to contain several distinct phases, all with very low apparent visible porosity. A dark, angular particle with a width of 90 μm had a high calcium intensity with the absence of potassium, EDX quantification provided a composition of $Ca_{0.8}[Al_{1.7}Si_2O_8]$, corresponding to anorthite (**N**). In Figure 4, A magnesium-calcium rich region yielded a more complex EDX composition of $Fe_{0.2}Al_{0.2}Mg_{0.8}Ca_{0.9}[Si_2O_6]$, indicating a diopsidian pyroxene with incorporation of small amounts of iron and aluminium, associated with the XRD phase match for pyroxene (**X**).

The bulk matrix phase encapsulating the crystal grains within the sample was reviewed, with EDX maps over two regions showing evenly distributed intensities for potassium and calcium as well as a high detection of aluminosilicate constituents. A bright globular 5–10 μm precipitate phase was abundant in the matrix and appeared to have a high Cs content. This matrix-precipitate complex appeared to have an

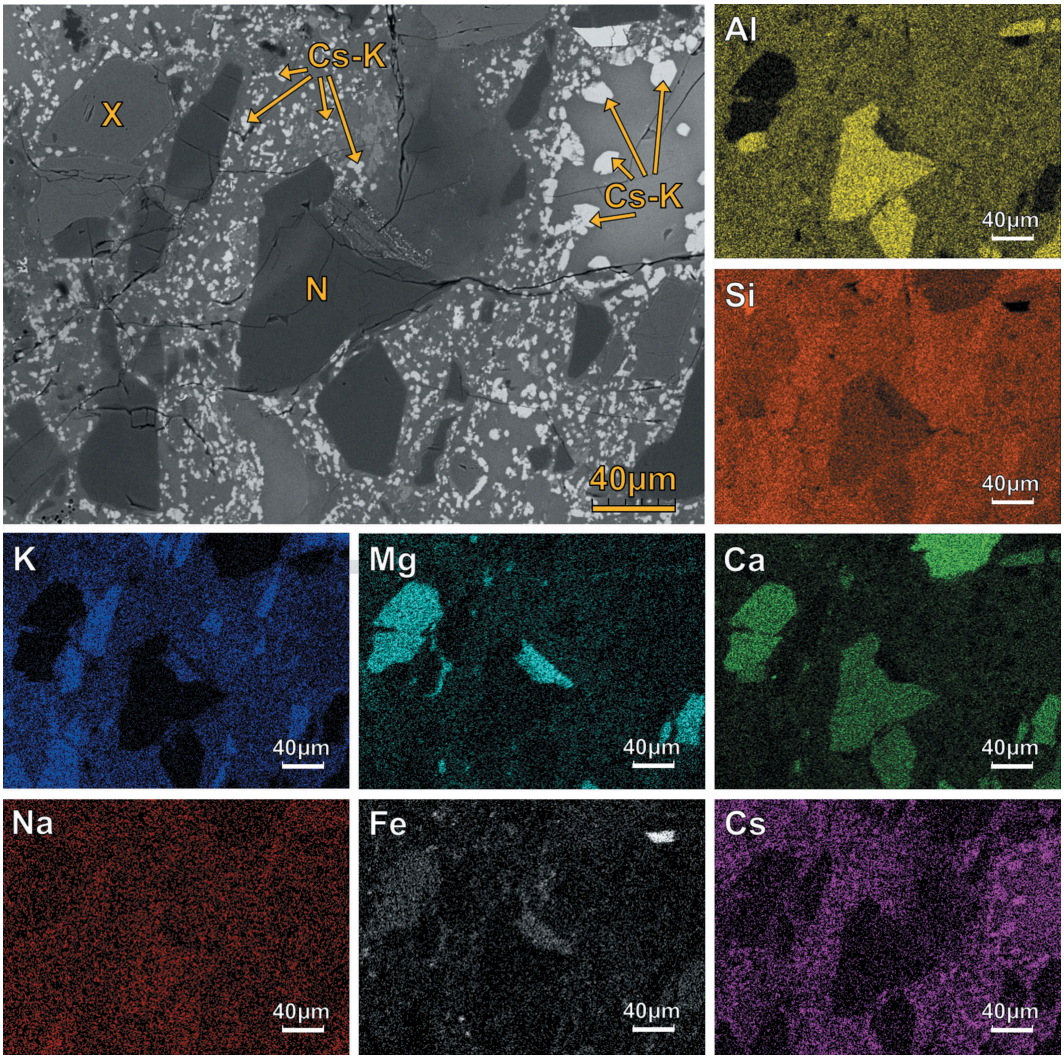

Figure 4. SEM/EDX micrographs of SPS-1 (1000°C, 10 min, 15 MPa), where labelled phases correspond to (N) anorthite, (X) pyroxene, and (Cs-K) cesium–potassium feldspars dispersed in anorthitic matrices.

intermediate potassium and plagioclase feldspar composition of $Cs_{0.7}Ca_{0.5}K_{1.1}[Al_3Si_8O_{22}]$, equating to a Cs waste-loading of 11.0 ± 2.8 wt.%. A breakdown of the cesium containing zeolite structure appears to have formed a combined matrix of the lower free energy alkali feldspars (**K** type and **Cs** type) [20] and anorthite, for which only limited powder diffraction reference data were available. Analysis of SPS-2 (Supporting Info 4) displays very similar features to the 15 MPa microstructure: namely a mixed feldspar-plagioclase composition of $Cs_{0.9}Ca_{0.5}K_{1.1}[Al_3Si_8O_{22}]$, corresponding to a Cs waste-loading capacity of 13.7 ± 4.2 wt.%. This indicated that pressure had little effect on the microstructure and local chemistry of the sintered wasteform.

In Figure 5, the higher temperature SPS-3 sample (1100°C) resulted in a noticeably sparser distribution of distinctive phase regions. The Cs-rich matrix (white precipitate) demonstrated the lowest cesium loading of the three SPS wasteforms, with a calculated composition of $Cs_{0.5}Ca_{0.3}K_{1.6}[Al_3Si_8O_{24}]$, which corresponds to a Cs waste-loading capability of 8.4 ± 3.3 wt.%. This could be indicative of a greater abundance of this phase or Cs incorporation into other phases (e.g. the vitreous phase). The remaining features of SPS-3 corresponding to a ~100 μm diameter dark, angular anorthite (**N**) particle with a formula $Ca_{0.8}[Al_{1.7}Si_2O_8]$ continue to remain out of the solid solution. The elongated particle with apparent delamination can be observed reacting with the matrix phase, where the bulk particle had an EDX quantified chemistry of $K_{0.8}[AlSi_3O_8]$, a K-feldspar (**K**), and that of the reaction-rim was $Ca_{0.2}K_{0.5}[AlSi_3O_8]$, a combination of plagioclase and K-feldspar (**K** + **N**).

Density balance measurements, Table 2, indicated that lower temperature sintering conditions (1000°C) gave the best density values, 2.658 ± 0.004 g/cm^3 for SPS-1 and 2.658 ± 0.003 g/cm^3 for SPS-2. The poorest density balance results were those of the SPS-3 sample, with an average of 2.588 ± 0.003 g/cm^3. The results for gas pycnometry of SPS samples were in agreement with the Archimedes balance data, showing that the optimum density was achieved with the lower sintering temperature of 1000°C and higher

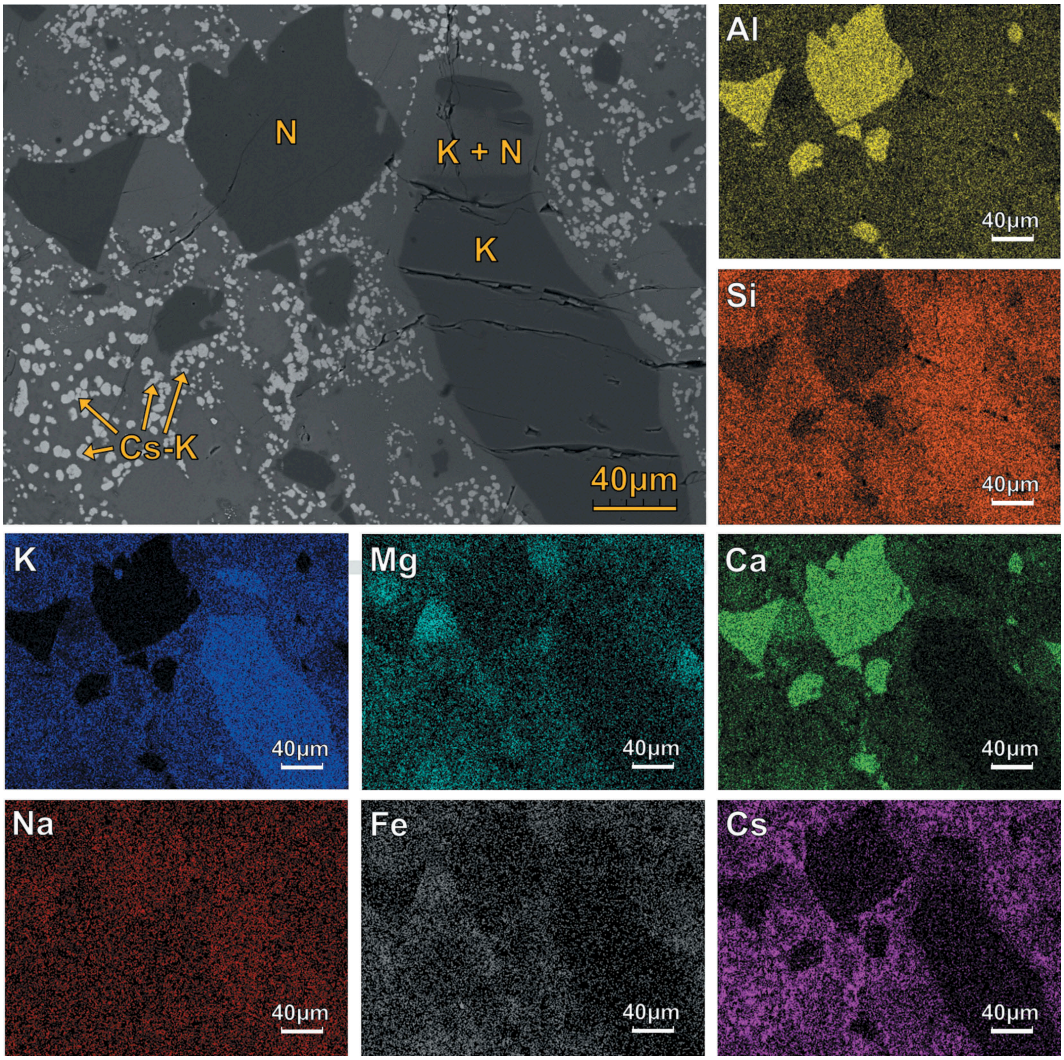

Figure 5. SEM/EDX micrographs of SPS-3 (1100°C, 10 min, 15 MPa), where labelled phases correspond to (K) potassium feldspar, (N) anorthite, and (Cs-K) cesium–potassium feldspars dispersed in anorthitic matrices.

pressure of 50 MPa, with 2.7314 ± 0.0017 g/cm^3. This corresponded to a 10.7% increase from the Cs-exchanged source material. The ground material from the SPS-3 pellet achieved poorer densities compared to the low temperature counterparts, which may have been due to a microstructural bloating effect resulting from the evolution of water [21]. Considering the measured average apparent density (see material synthesis) and the gas pycnometry results, the wasteform volume reductions achieved for SPS-1, 2 and 3 were 41.6 ± 1.0%, 43.0 ± 1.0% and 40.3 ± 1.0%, respectively. With the highest density and volume reduction, the SPS-2 material was selected as an optimal candidate for a 28-day chemical durability study.

3.3 Durability study of reactive spark plasma sintered material

The short-term chemical durability of Cs-chabazite processed as SPS-2 (1000°C/50 MPa) was performed using ASTM PCT-B methodology [15]. Figure 6 describes the normalised mass loss of elements as detected by ICP-OES (IC for Cs, standard deviations were obtained from duplicate samples). The average pH (day 0–28, 7 time points) during testing was observed to be pH 10.64 ± 0.24, and this low standard deviation indicated that the sample naturally buffered during experiment initialisation. In Figure 6, there was a high initial elemental release rate observed between day 0 and day 1, especially prominent for Si, Al, and Cs. This behaviour is associated with the rapid dissolution of residual fines within the sample, even though due care was taken to remove fines during sample preparation by washing with IPA until clear.

In Figure 6, the Si concentration (present at SiO_2 55.6 wt.%, Table 1) was observed to increase commensurate with experiment duration, indicative of accelerated dissolution for the SPS-2 sample. The normalised release rate for Si was calculated as 1.13 ± 0.12 × 10^{-3} g m^{-2} d^{-1}, day 28 was excluded due to significant evaporation of the leaching solution. In comparison, clinoptilolite simulant converted into $NaAlO_2$ and NaB_4O_7-based glasses (via hot isostatic pressing) resulted in Si release

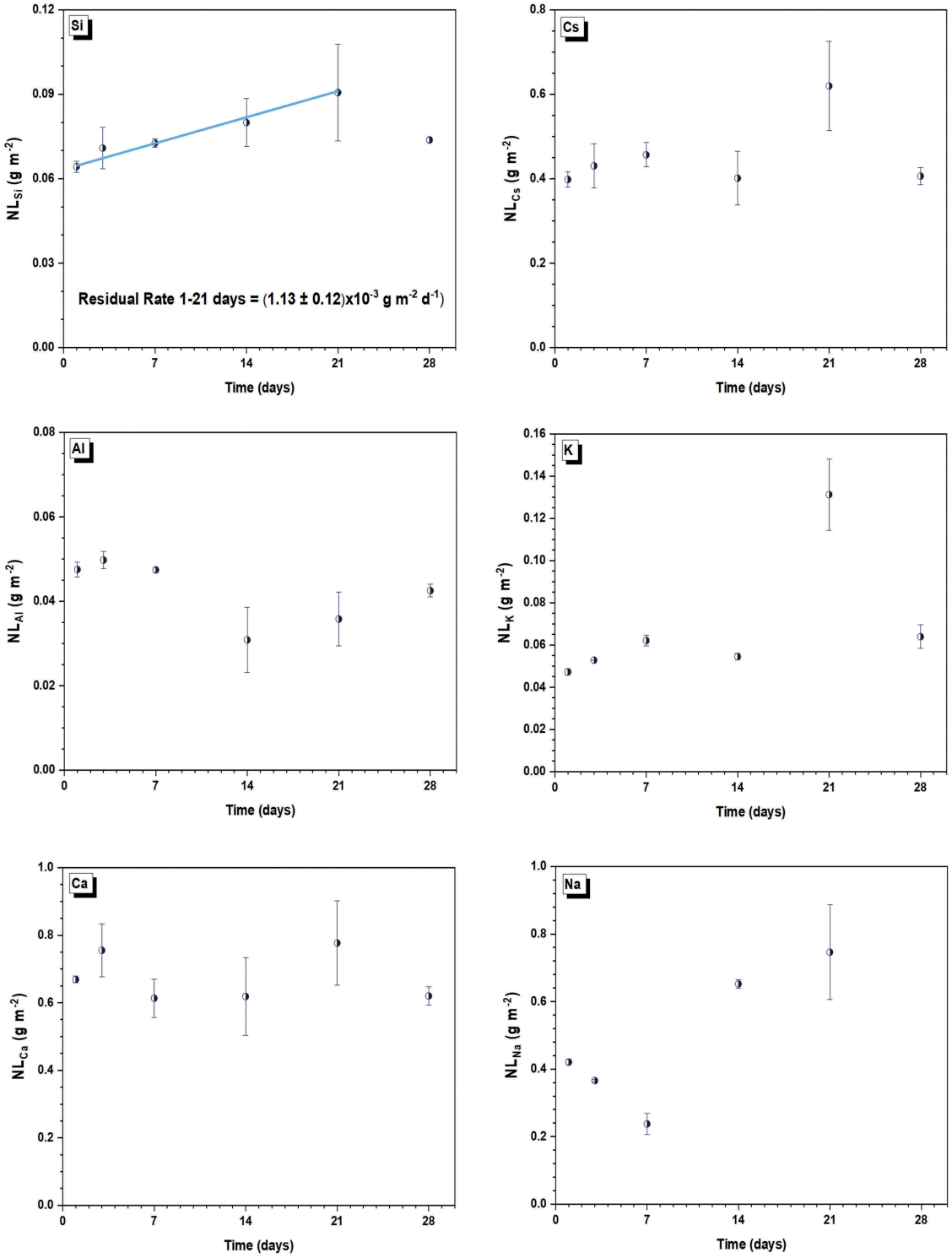

Figure 6. Normalised elemental mass loss of SPS-2 (1000°C, 10 min, 50 MPa) from PCT-B experiments performed at 90°C in 18.2 MΩ water.

rates of 4.21×10^{-4} g m^{-2} d^{-1} and 6.80×10^{-4} g m^{-2} d^{-1}, respectively [22]. Prototype fast reactor (PFR) raffinate immobilised in a barium borosilicate glass achieved a Si release rate of 7.19×10^{-3} g m^{-2} d^{-1} [23]. The durability of SPS-2 is therefore comparable to proposed thermal treatment options for two different UK ILW waste streams; however, it should be noted that the cited examples were performed at a higher SA/V ratio (2000 m^{-1}) than this study. The Cs-chabazite immobilised in SPS-2 resulted in a multi-phase matrix with Si present in all of the crystalline phases (K-feldspar, leucite, anorthite, and pyroxene) and the vitreous phase, which makes it difficult to assign dissolution to a specific phase within the sample.

A general trend was observed for the dissolution behaviour of Al, Ca, Cs, and K (Figure 6), where the concentrations appeared to remain steady throughout the duration (within error). This would suggest the

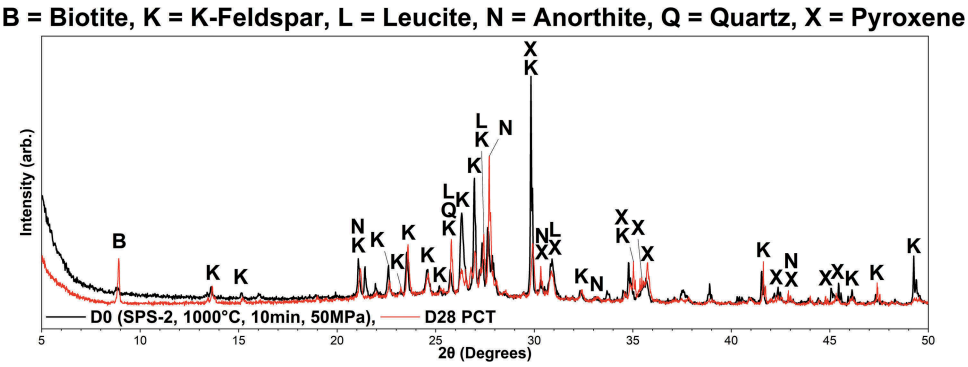

Figure 7. XRD pattern for the SPS-2 (1000°C, 10 min, 50 MPa) before and post-dissolution at day 0 and 28.

sample underwent congruent/constant dissolution. It is considered that the elemental loss spikes observed at day 21 could be associated with the evaporative loss resulting in artificially increased concentrations. XRD performed post-dissolution (Figure 7) revealed that the relative intensity of K-feldspar reflections significantly reduced compared to those for anorthite. The relative intensity of the biotite reflection at ~9° 2θ increased compared to the SPS-2 before dissolution (Figure 3). As no further thermal treatment process occurred to this sample, it could be assumed that the overall degree of crystallinity decreased as a result of the experiment rather than an increased presence of biotite.

Analysis of the Cs-chabazite SPS-2 particles post-dissolution by SEM/EDX (Figure 8) demonstrates that the dissolution of the material occurs heterogeneously, with preferential alteration of some phases. Within the central particle, regions rich in Ca, Al, and Si are representative of anorthite concurring with the XRD (Figure 3) for the continued presence of anorthite. The micro-cracks observed across several particles are from sample preparation rather than dissolution effects, shown in Figures 4 and 5.

The greyscale differences in the central particle elucidate the presence of two Cs-bearing K-feldspar regions with differing behaviour under dissolution conditions. The first K-feldspar can be assigned to the light grey region (surrounding the anorthite grain and left-hand side particles), where no dissolution effects were observed. The composition of this region was determined to be $Cs_{0.3}Mg_{0.4}Ca_{0.6}K_{0.9}[Al_{3.4}Si_8O_{22}]$, with a Cs concentration of 5.8 ± 1.8 wt.%. In contrast, the development of pitting/visible porosity was observed within the darker grey region (central particle, bottom left) suggestive of preferential dissolution. The calculated composition post-dissolution was $Cs_{0.1}Na_{0.2}Mg_{0.4}Ca_{0.2}Fe_{0.2}K_{2.0}[Al_{3.3}Si_8O_{22}]$, with a Cs concentration of 1.0 ± 0.4 wt.%. Due to the complex nature of a multi-phase wasteform, future work to observe the retreat rate of the component phases by vertical scanning interferometry (VSI) and perform micro-analysis techniques to identify the phases would help to determine the driving mechanism behind the dissolution behaviour observed in this study.

4. Conclusions

Microstructural characterisation and phase assemblage revealed the diverse mineral composition of a natural chabazite source used as a simulant for spent ion exchange media arising on the Fukushima NPP site. A proof of concept study demonstrated the efficacy of SPS for conditioning of such aluminosilicate zeolite wastes. Conceptual wasteforms were successfully produced using different SPS conditions, where the collapse of the porous zeolite framework led to an increase in absolute density. The highest Cs waste loading (in the main Cs-bearing phase) was obtained at sintering conditions of 1000°C/50 MPa. The uniaxial application of pressure and high temperature for 10 min provides a combination of parameters, which was ideal for ensuring collapse of the chabazite framework with partitioning of the exchanged Cs into a feldspar phase. The long-term durability of the SPS-2 sample is challenging to understand due to the heterogeneous nature of the sample and requires further work to understand the contributions of the component phases to the overall dissolution behaviour. Although use of this technology for waste conditioning is at a stage of relative infancy and Technology Readiness Level of 2–3, SPS has the potential for high volume reduction of wastes, providing a significant advantage over cement encapsulation, due to the anticipated waste volume increase and potential waste / encapsulant reaction. The process is the markedly faster and less energy intensive than hot isostatic pressing, at comparable lab scale. Some limited scalability studies for ceramic-metal type functionally graded materials were reported by Gullion *et al.* and Tokita who demonstrated capability for homogenous consolidation of disc-shaped samples with up to 100 mm diameter and 40 mm thickness [24–26]. Clearly, considerable additional research would be required to translate the conceptual approach developed here to application at full scale for

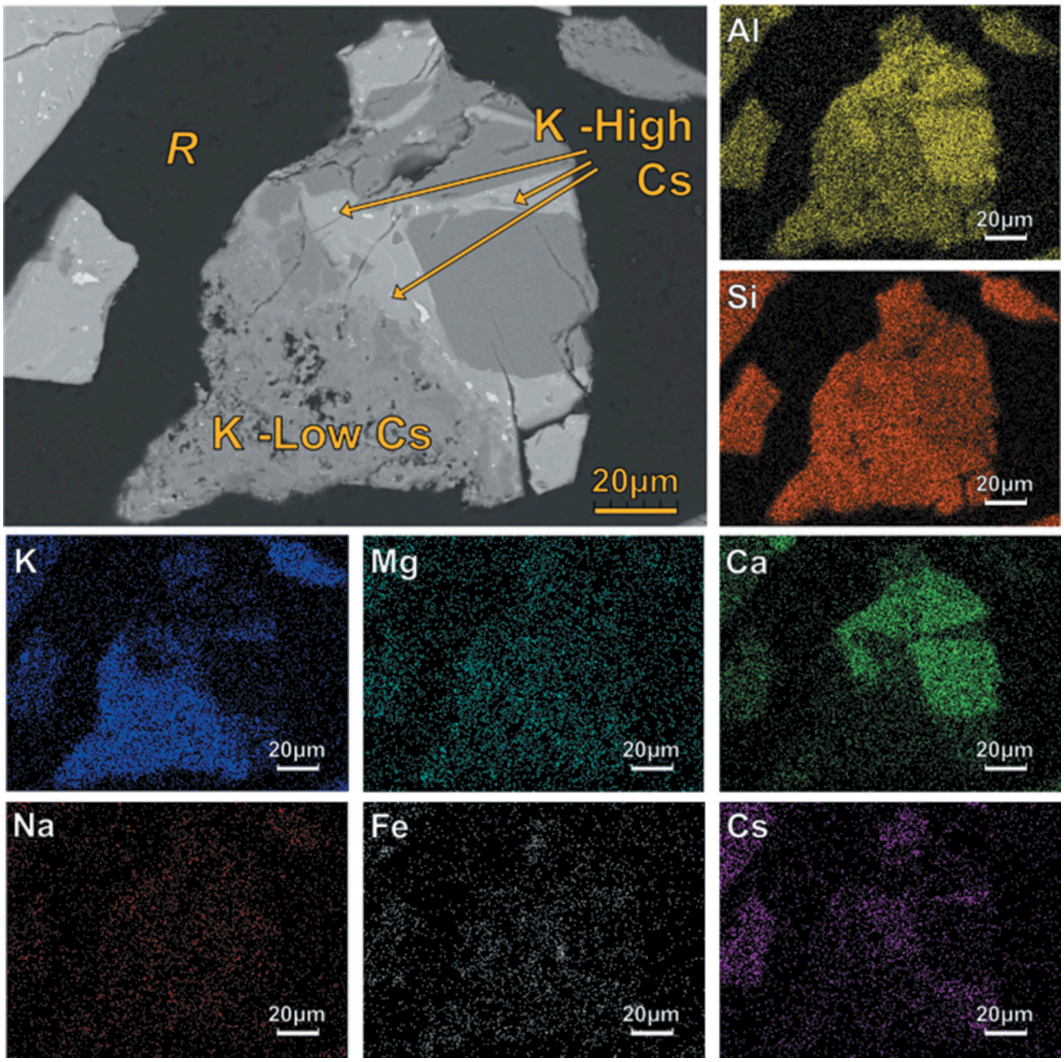

Figure 8. SEM/EDX micrographs of SPS-2 (1000°C, 10 min, 50 MPa) post-dissolution at day 28.

conditioning of inorganic ion exchange materials. Nevertheless, the full retention of the Cs_2O inventory in processing and durability experiments achieved in this conceptual study provide a compelling case for such future research. Although the product geometry, in the form of large sintered discs, might be considered a limitation, such geometry would offer the potential to control the thermal characteristics of the waste package by separating such discs with thermally conductive materials. Future work should use a more realistic simulant to allow for more accurate modelling and characterisation, and the radiation stability of the wasteforms should then be assessed.

Acknowledgments

The authors are grateful to the EPSRC for sponsorship of this research, under grants EP/N017617/1, EP/P013600/1, EP/S01019X/1, and EP/N017870/1. LH is grateful to EPSRC and the Nuclear Decommissioning Authority for award of a PhD studentship. This research was performed in part at the MIDAS Facility, at the University of Sheffield, which was established with support from the Department of Energy and Climate Change.

Disclosure statement

No potential conflict of interest was reported by the authors.

Funding

This work was supported by the Engineering and Physical Sciences and Research Council (EPSRC) [EP/N017617/1, EP/P013600/1, EP/S01019X/1, EP/N017870/1.].

ORCID

Liam. C. Harnett http://orcid.org/0000-0002-9296-1145
Laura. J. Gardner http://orcid.org/0000-0003-3126-2583
Shi-Kuan Sun http://orcid.org/0000-0002-1688-5072
Colleen Mann http://orcid.org/0000-0002-8781-1652
Neil. C. Hyatt http://orcid.org/0000-0002-2491-3897

References

[1] Tokyo Electric Power Company. Fukushima nuclear accident analysis report. Toyko, Japan: Tokyo Electric Power Company Holdings, Inc.; 2012.

[2] Denton MS, Mertz JL, Bostick WD, editors. Fukushima nuclear crisis recovery: a modular water treatment system deployed in seven weeks. AZ, USA: Waste Management; 2012 Feb 26 - March 1.
[3] Baek W, Ha S, Hong S, et al. Cation exchange of cesium and cation selectivity of natural zeolites: chabazite, stilbite, and heulandite. Microporous Mesoporous Mater. 2018;264:159–166.
[4] Calligaris M, Mezzetti A, Nardin G, et al. Crystal structures of the hydrated and dehydrated forms of a partially cesium-exchanged chabazite. Zeolites. 1986;6(2):137–141.
[5] Tokyo Electric Power Company. Situation of storage and treatement of accumulated water including highly concencentrated radioactive materials and Fukushima Daiichi nuclear power station (372nd release) - October 4th, 2018. Toyko, Japan: Tokyo Electric Power Company Holdings, Inc; 2018.
[6] International Atomic Energy Agency. Application of ion exchange processes for the treatment of radioactive waste and management of spent ion exchangers. Technical repors series no. 408. Vienna, Austria: International Atomic Energy Agency; 2002.
[7] Kimura R, Inagaki Y, Idemitsu K, et al. Vitrification processes of simulated cesium sorbing zeolite waste. Prog Nucl Energy. 2018;108:497–502.
[8] Gordon LE, Milestone NB, Angus MJ, editors. The immobilisation of clinoptilolite within cementitious systems. Materials Research Symposium; Boston, USA. 2008.
[9] Sharp JH, Milestone NB, Hill J, et al., editors. Cementitious systems for encapsulation of intermediate level waste. The 9th International Conference on Radioactive Waste Management and Environmental Remediation; 2003 Sept 21-25; Oxford, UK.
[10] Milestone NB. Reactions in cement encapsulated nuclear wastes: need for toolbox of different cement types. Adv Appl Ceram. 2006;105(1):13–20.
[11] Jenni A, Hyatt NC. Encapsulation of caesium-loaded Ionsiv in cement. Cem Conc Res. 2010;40:1271–1277. https://doi.org/10.1016/j.cemconres.2009.10.015
[12] Munir ZA, Anselmi-Tamburini U, Ohyanagi M. The effect of electric field and pressure on the synthesis and consolidation of materials: A review of the spark plasma sintering method. J Mater Sci. 2006;41(3):763–777.
[13] Verdi SPA. Zeover data sheet. Torrino, Italy: Verdi S. p.A; 2015.
[14] Sun S-K, Stennett MC, Corkhill CL, et al. Reactive spark plasma synthesis of $CaZrTi_2O_7$ zirconolite ceramics for plutonium disposition. J Nucl Mater. 2018;500:11–14.
[15] ASTM International. C 1285 – 02 (Reapproved 2008) standard test methods for determining chemical durability of nuclear, hazardous, and mixed waste glasses and multiphase glass ceramics: the Product Consistency Test (PCT). USA.
[16] Du T, Fang X, Wei Y, et al. Synthesis of nanocontainer chabazites from fly ash with a template- and fluoride-free process for cesium ion adsorption. Energy Fuels. 2017;31(4):4301–4307.
[17] Greaves GN, Meneau F, Kargl F, et al. Zeolite collapse and polyamorphism. J Phys. 2007;19(41):415102.
[18] Belviso C. EMT-type zeolite synthesized from obsidian. Microporous Mesoporous Mater. 2016;226:325–330.
[19] Schairer JF, Bowen NL. Melting relations in the systems Na_2O-Al_2O_3-SiO_2 and K_2O-Al_2O_3-SiO_2. Am J Sci. 1947;245(4):199–201.
[20] Rajib M, Sasaki T, Kobayashi T, et al. Analysis of sorption behavior of cesium and iodide ions on pumice tuff. J Nucl Sci Technol. 2011;48(6):950–957.
[21] De' Gennaro R, Cappelletti P, Cerri G, et al. Zeolitic tuffs as raw materials for lightweight aggregates. Appl Clay Sci. 2004;25(1):71–81.
[22] Heath PG. Alternative procesing methids for the thermal treatment of radioactive wastes [PhD Thesis]. Sheffield: The University of Sheffield; 2015.
[23] Heath PG, Corkhill CL, Stennett MC, et al. Whales KM and Hyatt NC. Immobilisation of prototype fast reactor raffinate using barium silicate ILW glasses. J Nucl Mater. 2018;508:203–211.
[24] Tokita M. Development of large-size ceramic/metal bulk FGM fabricated by spark plasma sintering. Proc 1998 5th Int Symp Functionally Graded Mat. 1999;308-311:83–88.
[25] Tokita M. Large-size WC/Co functionally graded materials fabricated by spark plasma sintering (SPS) method. Proc Seventh Int Symp Functionally Graded Mat. 2003;423-425:39–44.
[26] Guillon O, Gonzalez-Julian J, Dargatz B, et al. Field-assisted sintering technology/spark plasma sintering: mechanisms, materials, and technology developments. Adv Eng Mater. 2014;16(7):830–849.